STOKES FLOW INDUCED DRAG AND TORQUE ON ASBESTOS-LIKE FIBRES CANNOT BE ESTIMATED BY A SIMPLISTIC ELLIPSOIDAL APPROXIMATION

JURE RAVNIK[1], MITJA ŠTRAKL[1], JANA WEDEL[2], PAUL STEINMANN[2,3] & MATJAŽ HRIBERŠEK[1]
[1]Faculty of Mechanical Engineering, University of Maribor, Slovenia
[2]Institute of Applied Mechanics, Friedrich-Alexander Universität Erlangen-Nürnberg, Germany
[3]Glasgow Computational Engineering Centre, University of Glasgow, UK

ABSTRACT
In this paper we present an algorithm based on the Boundary Element Method for solving the Stokes flow around an arbitrarily shaped particle in multiphase flows. The objective of the algorithm is to determine the exact drag force and torque experienced by the particle during its motion in a turbulent flow field. The developed method is used to compare the predicted force and torque values on a realistic 3D model of a mineral fibre and its simplifying ellipsoidal approximation. We found that the force and torque values calculated for the real particle geometry differ greatly from the values obtained with the simplifying ellipsoidal approximation. On average, a relative error of less than 10% is achieved for only 10%–30% of the particle orientations.
Keywords: boundary element method, multiphase flows, Lagrangian simulation, mineral, asbestos, muscovite.

1 INTRODUCTION

Asbestos is a term used to describe a group of six fibrous silicate minerals (Strohmeier et al. [1]) that have an asbestiform habit and are and were used commercially. It is still widely used and associated with disease. In particulate form, it takes the form of fibre-like structures which, when suspended in the air, can be inhaled and enter the lungs. The asbestos fibres in question are small, with a length in the micrometre range and a length-to-width ratio of more than three. The translational and rotational dynamics of such small particles are primarily determined by the airflow surrounding them. Their Stokes number is small, so they react quickly to changes in the air flow and can therefore remain in the air for a long time. For this reason, it is almost impossible to completely avoid exposure to asbestos. Our inability to smell, touch, see or otherwise identify asbestos fibres is the main reason why so many people have been unable to detect avoid exposure to the carcinogenic substance.

Many researchers [2]–[4] model asbestos fibres as elongated ellipsoids. In reality [5]–[8], however, the shape of the particle can be curved, rod-shaped and contain protrusions, so the simplifying ellipsoid approximation can be questionable. In this paper, we compare the drag and torque exerted on a fibre using a 3D model of a realistic asbestos-like mineral and its simplifying ellipsoidal approximation by means of BEM-based numerical simulation.

Because the asbestos particles are so small, they follow the airflow almost completely. The relative velocity of the air experienced by the particles is small. If we consider this problem as a flow over a blunt body, we find that we are dealing with a micrometre-sized body ($d \approx 10^{-6}m$), a small air velocity $= |\vec{v}_0| \ll 1m/s$ and air of known viscosity ($\nu \approx 10^{-5}m^2/s$) as the fluid. It is obvious that the particle Reynolds number for asbestos fibres in air is much smaller than one. This means that we can approximate the air flow field around the particle by considering only the diffusive transport of momentum and neglecting the convective transport of momentum. Such an approximation leads to the Stokes equations for fluid flow. These can be written in terms of a boundary integral and a BEM algorithm

can be developed to find solutions to such problems. In the following we present such an algorithm.

2 GOVERNING EQUATIONS

2.1 The particle

We consider a particle of volume V in a fluid. The spherical volume equivalent radius of the particle is $R = (3V/4\pi)^{1/3}$. The force and torque on such a particle due to the presence of a fluid can be calculated by

$$\vec{F} = \int_\Gamma \vec{q} d\Gamma, \qquad \vec{T} = \int_\Gamma \vec{r} \times \vec{q} d\Gamma, \tag{1}$$

where $\vec{q} = \underline{\sigma} \cdot \vec{n}$ is the boundary traction, Γ the surface of the particle and $\vec{r}$ the position vector in particle frame of reference (FoR). The boundary traction represents the sink of momentum at the particle surface and thus its integral over the surface yields the force. In case of a sphere moving in a still fluid, this force evaluates to $\vec{F} = 6\pi R\mu\vec{u}$. When a sphere spins in still fluid, it generates torque of $\vec{T} = 8\pi R^3\mu\vec{\omega}$. This expression can be used to non-dimensionalize the force and torque action on a particle in a moving fluid by $F_0 = \pi\mu R v_0$ and $T_0 = \pi R^3\mu v_0/\mathcal{L}$ with v_0 and $\mathcal{L}$ characteristic velocity and length scale of the flow.

We assume the particle is located in an unsteady turbulent or laminar flow. Let the flow velocity in inertial FoR be denoted by $\vec{v}$. We assume that:

- the particle is small enough, that the particle Reynolds number: $Re_p = |\vec{v}_0|R/\nu \ll 1$. Here $\vec{v}_0$ is the relative flow velocity at the location of the particle.
- the particle is small enough, that flow shear (velocity gradient tensor) is linear in the vicinity of the particle. The following is valid $||\vec{\nabla}\vec{v}||_F \ll |\vec{v}_0|/R$. Here $||\vec{\nabla}\vec{v}||_F$ is the Frobenius norm of the velocity gradient tensor calculated at the particle location. At the same time the particle shear Reynolds number $Re_G = R^2||\vec{\nabla}\vec{v}||_F/\nu \ll 1$.
- the particle is much smaller that the Kolomogorov length scale, i.e. it is much smaller that the size of the smallest eddy in the flow field.

With these assumptions the flow field as seen from the perspective of the particle is governed by the Stokes equation. Furthermore, to facilitate finding the boundary conditions for our numerical solver, we model the undisturbed flow field around the particle with linear shear. Thus, the linearised flow velocity $\vec{w}$ in the inertial FoR with the origin at the particle centre can be written as:

$$\vec{w} = \vec{v}_0 + (\vec{\nabla}\vec{v})_0 \cdot \vec{r}, \tag{2}$$

where $\vec{v}_0$ is the flow velocity at the position of the particle and $(\vec{\nabla}\vec{v})_0$ is the flow velocity gradient tensor at the position of the particle and $\vec{r} = (x, y, z)$ is the location vector the inertial FoR with the origin at the particle centre. See Fig. 1 for details. Eqn. (2) is written in the inertial FoR with the origin set to the particle location, so $\vec{w}(0,0,0)$ and $(\vec{\nabla}\vec{w})(0,0,0)$ produce values consistent with $\vec{v}$ and $(\vec{\nabla}\vec{v})$ at the location of the particle.

The particles can have any orientation. It is convenient to create the numerical grid for only one particle orientation and express the flow velocity field in the particle FoR. In this way we can avoid having to rotate the computational grid for each particle orientation and re-evaluate the integrals to form the system of linear equations. It is better to rotate the input velocity, which is given as a boundary condition.

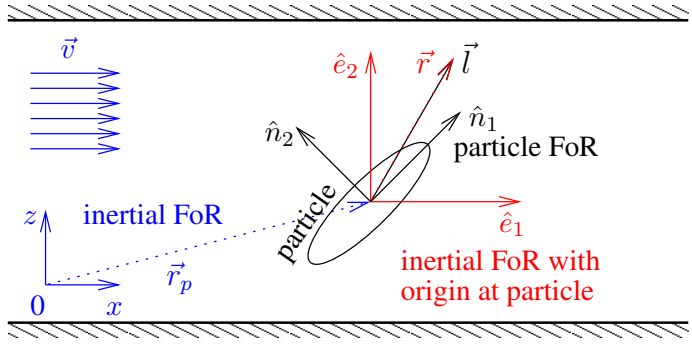

Figure 1: A particle in a flow field. In the inertial reference frame (blue) the flow velocity is $\vec{v}$ and the particle is at $\vec{r}_p$. The linearised flow field $\vec{w}$ is written in the inertial reference frame with origin in the particle centre (red). The particle reference frame (black) is defined by the orientation of the particle. The linearised flow velocity in the particle reference frame is $\vec{u}$. $\vec{r}$ and $\vec{l}$ indicate the location of interest in the inertial reference frame with origin in the particle centre and the particle reference frame, respectively.

Let us assume the inertial FoR is defined by basis vectors $\hat{e}_1$, $\hat{e}_2$, and $\hat{e}_3$ while the particle orientation in the same frame of reference is defined by basis vectors $\hat{n}_1$, $\hat{n}_2$, and $\hat{n}_3$. We compute $\hat{e}_4 = \hat{e}_1 \times \hat{e}_3$ and $\hat{n}_4 = \hat{n}_1 \times \hat{n}_3$ and obtain the rotation matrix as:

$$\underline{R} = \begin{pmatrix} \hat{e}_{1,x} & \hat{e}_{3,x} & \hat{e}_{4,x} \\ \hat{e}_{1,y} & \hat{e}_{3,y} & \hat{e}_{4,y} \\ \hat{e}_{1,z} & \hat{e}_{3,z} & \hat{e}_{4,z} \end{pmatrix} \cdot \begin{pmatrix} \hat{n}_{1,x} & \hat{n}_{1,y} & \hat{n}_{1,z} \\ \hat{n}_{3,x} & \hat{n}_{3,y} & \hat{n}_{3,z} \\ \hat{n}_{4,x} & \hat{n}_{4,y} & \hat{n}_{4,z} \end{pmatrix}. \tag{3}$$

Alternatively, if the particle orientation is expressed in terms of Euler parameters (e_0, e_1, e_2, e_3), as it is common in Lagrangian particle tracking algorithms, the same rotation matrix written in terms of the Euler parameters is

$$\underline{R} = \begin{pmatrix} e_0^2 + e_1^2 - e_2^2 - e_3^2 & 2(e_1e_2 + e_0e_3) & 2(e_1e_3 - e_0e_2) \\ 2(e_1e_2 - e_0e_3) & e_0^2 - e_1^2 + e_2^2 - e_3^2 & 2(e_2e_3 + e_0e_1) \\ 2(e_1e_3 + e_0e_2) & 2(e_2e_3 - e_0e_1) & e_0^2 - e_1^2 - e_2^2 + e_3^2 \end{pmatrix}. \tag{4}$$

The transpose of the rotation matrix may be used to find the particle basis, i.e. $\hat{n}_1 = \underline{R}^T \hat{e}_1$. With the rotation matrix we can express the velocity field in the particle FoR as

$$\vec{u} = \underline{R} \cdot \vec{w}. \tag{5}$$

Considering a point in the particle FoR $\vec{l}$, the velocity in particle FoR is then calculated as

$$\vec{u} = \underline{R} \cdot \left[\vec{v}_0 + (\vec{\nabla}\vec{v})_0 \cdot \underline{R}^T \cdot \vec{l} \right] \tag{6}$$

since $\vec{r} = \underline{R}^T \cdot \vec{l}$ is the location of the chosen point in the inertial FoR with the origin at the particle. This means, that the force and torque experienced by a particle can be uniquely defined using the particle orientation $\underline{R}$, the fluid velocity at the position of the particle $\vec{v}_0$ and the fluid velocity gradient tensor at the position of the particle $(\vec{\nabla}\vec{v})_0$.

2.2 The fluid governing equations in the particle FoR

We consider the steady incompressible flow of a Newtonian fluid at very small Reynolds numbers, i.e. $Re \ll 1$, where we can neglect the advection term in the Navier–Stokes equations, leading to the equations of creeping flow (Stokes):

$$\vec{\nabla} \cdot \vec{u} = 0, \qquad \vec{\nabla} \cdot \underline{\sigma} + \rho \vec{g} = 0. \tag{7}$$

Here $\vec{u}$ is the flow velocity, ρ is the fluid density and $\vec{g}$ is the gravitational acceleration. The Cauchy stress tensor $\underline{\sigma}$ is defined as $\underline{\sigma} = -P\underline{I} + \underline{\tau}$, where P is the pressure, $\underline{I}$ the identity tensor, and $\underline{\tau}$ the viscous stress tensor. A Newtonian model for the viscous stress tensor $\tau_{ij} = \mu \left[\frac{\partial u_i}{\partial x_j} + \frac{\partial u_j}{\partial x_i} \right]$ leads to the following form of the Stokes equation:

$$-\vec{\nabla} P + \mu \nabla^2 \vec{u} + \rho \vec{g} = 0, \tag{8}$$

where μ is the fluid viscosity. Finally, we recognise, that gravity is a conservative force, which may be written as a gradient of the gravitational potential and introduce a modified pressure as $p = P - \rho\Phi$, where $\vec{g} = \vec{\nabla}\Phi$. With this, the final form of the Stokes equation is

$$-\vec{\nabla} p + \mu \nabla^2 \vec{u} = 0. \tag{9}$$

3 BOUNDARY INTEGRAL EQUATIONS

3.1 Green's functions

The Stokes flow Green's functions satisfy the continuity equation $\vec{\nabla} \cdot \vec{u} = 0$ and are the solutions of the singularly forced Stokes equation. Defining $\hat{r} = \vec{r} - \vec{r}_0$ and $r = |\hat{r}|$ the 3D free-space Green's functions are

$$\mathcal{G}_{ij} = \frac{\delta_{ij}}{r} + \frac{\hat{r}_i \hat{r}_j}{r^3}, \quad \mathcal{P}_j = 2\frac{\hat{r}_j}{r^3}, \quad \mathcal{T}_{ijk} = -6\frac{\hat{r}_i \hat{r}_j \hat{r}_k}{r^5}, \quad \mathcal{K}_{ij} = -4\frac{\delta_{ij}}{r^3} + 12\frac{\hat{r}_i \hat{r}_j}{r^5}. \tag{10}$$

3.2 Velocity field

The boundary integral representation for the Stokes problem is [9]

$$c(\vec{r}_0) u_j(\vec{r}_0) = \int_\Gamma^{PV} u_i(\vec{r}) \mathcal{T}_{ijk}(\vec{r}, \vec{r}_0)\, n_k(\vec{r}) d\Gamma(\vec{r}) - \frac{1}{\mu} \int_\Gamma \mathcal{G}_{ji}(\vec{r}, \vec{r}_0)\, q_i(\vec{r}) d\Gamma(\vec{r}), \tag{11}$$

where $c(\vec{r}_0) = 2\alpha$ is twice the solid angle as seen from the point $\vec{r}_0$, i.e. in the interior of the domain $c = 8\pi$, at a smooth boundary $c = 4\pi$. The normal vector $\vec{n}$ points into the domain. The terms on the right represent the double and single layer potentials of the three-dimensional Stokes flow. To derive a discrete version of eqn (11) we consider the boundary $\Gamma = \sum_l \Gamma_l$ to be decomposed into boundary elements Γ_l:

$$c(\vec{r}_0) u_j(\vec{r}_0) = \sum_l \int_{\Gamma_l}^{PV} u_i(\vec{r}) \mathcal{T}_{ijk}(\vec{r}, \vec{r}_0)\, n_k^{(l)} d\Gamma(\vec{r}) - \frac{1}{\mu} \sum_l \int_{\Gamma_l} \mathcal{G}_{ji}(\vec{r}, \vec{r}_0)\, q_i(\vec{r}) d\Gamma(\vec{r}), \tag{12}$$

where $n_k^{(l)}$ is the k component of the normal vector pointing from boundary element l into the domain.

Let Φ and Ψ be the interpolation functions used to interpolate the function and flux values within boundary elements, i.e. $u_i = \sum_m \Phi_m u_i^{(l,m)}$ and $q_i = \sum_m \Psi_m q_i^{(l,m)}$, where $u_i^{(l,m)}$ is the m^{th} nodal value of function within l^{th} boundary element. This yields

$$c(\vec{r}_0)u_j(\vec{r}_0) = \sum_l \sum_m u_i^{(l,m)} \int_{\Gamma_l}^{PV} \Phi_m \mathcal{T}_{ijk}\left(\vec{r},\vec{r}_0\right) n_k^{(l)} d\Gamma(\vec{r}) \\ -\frac{1}{\mu} \sum_l \sum_m q_i^{(l,m)} \int_{\Gamma_l} \Psi_m \mathcal{G}_{ji}\left(\vec{r},\vec{r}_0\right) d\Gamma(\vec{r}). \tag{13}$$

The following integrals must be calculated for each boundary element:

$$T_{ij}^{(l,m)}(\vec{r}_0) = \int_{\Gamma_l}^{PV} \Phi_m \mathcal{T}_{ijk}\left(\vec{r},\vec{r}_0\right) n_k^{(l)} d\Gamma \\ G_{ij}^{(l,m)}(\vec{r}_0) = \int_{\Gamma_l} \Psi_m \mathcal{G}_{ij}\left(\vec{r},\vec{r}_0\right) d\Gamma. \tag{14}$$

So, for a source point $(\vec{r}_0)$ we may write

$$c(\vec{r}_0)u_j(\vec{r}_0) = \sum_l \sum_m u_i^{(l,m)} T_{ij}^{(l,m)}(\vec{r}_0) - \frac{1}{\mu} \sum_l \sum_m q_i^{(l,m)} G_{ji}^{(l,m)}(\vec{r}_0). \tag{15}$$

Since the boundary elements share nodes, the number of integrals that need to be stored is actually less than $l \cdot m$. The integrals, which are required by the same node, can be summed up. The number of integrals values we store in memory is equal to the number of nodes in a mesh. When we place the source point in all boundary nodes, and store the integral values in matrices (the rows correspond to different source points, the columns to the different nodes in the mesh), we obtain the following systems of equations:

$$\{u_x\}[[T_{xx}] - c[I]] + \{u_y\}[T_{yx}] + \{u_z\}[T_{zx}] = \frac{1}{\mu}[\{q_x\}[G_{xx}] + \{q_y\}[G_{xy}] + \{q_z\}[G_{xz}]]. \tag{16}$$

$$\{u_x\}[T_{xy}] + \{u_y\}[[T_{yy}] - c[I]] + \{u_z\}[T_{zy}] = \frac{1}{\mu}[\{q_x\}[G_{yx}] + \{q_y\}[G_{yy}] + \{q_z\}[G_{yz}]]. \tag{17}$$

$$\{u_x\}[T_{xz}] + \{u_y\}[T_{yz}] + \{u_z\}[[T_{zz}] - c[I]] = \frac{1}{\mu}[\{q_x\}[G_{zx}] + \{q_y\}[G_{zy}] + \{q_z\}[G_{zz}]]. \tag{18}$$

Here the curly and square brackets denote nodal vectors of field functions and matrices of integrals, respectively. Known values of velocity or boundary traction can be used as boundary conditions. Collocation points are placed only into nodes, where the value is unknown. A system of linear equations is set up for all unknowns, where in case of unknown $\{u_x\}$ or $\{q_x\}$ eqn (16) is used, in case of unknown $\{u_y\}$ or $\{q_y\}$ eqn (17) is used and in case of unknown $\{u_z\}$ or $\{q_z\}$ eqn (18) is used.

3.3 Pressure field

The boundary integral equation to evaluate pressure in the domain given known velocity and traction at the boundary is

$$c(\vec{r}_0)p(\vec{r}_0) = \mu \int_\Gamma u_i(\vec{r}) \mathcal{K}_{ij}\left(\vec{r},\vec{r}_0\right) n_j(\vec{r}) d\Gamma(\vec{r}) - \int_\Gamma \mathcal{P}_i\left(\vec{r},\vec{r}_0\right) q_i(\vec{r}) d\Gamma(\vec{r}). \tag{19}$$

When the pressure evaluation point $\vec{r}_0$ is in the domain $c(\vec{r}_0) = 8\pi$. In the case $\vec{r}_0$ is at a smooth boundary, $c(\vec{r}_0) = 4\pi$, and the equation becomes hypersingular. In this case the second integral in eqn (19) exists only in the Cauchy principal value sense. However, because of the $1/r^3$ singularity in the kernel function $\mathcal{K}_{ij}$, the first integral exists only in the sense of the finite-part integral. Ingber and Li [10] proposed a regularization of the finite-part integral:

$$\mu(\vec{r}_0)p(\vec{r}_0) = \mu \int_\Gamma \left[u_i(\vec{r}) - u_i(\vec{r}_0)\right] \mathcal{K}_{ij}\left(\vec{r}, \vec{r}_0\right) n_j(\vec{r}) d\Gamma(\vec{r}) - \int_\Gamma \mathcal{P}_i\left(\vec{r}, \vec{r}_0\right) q_i(\vec{r}) d\Gamma(\vec{r}). \tag{20}$$

Both integrals in eqn (20) can be interpreted in the Cauchy principal value sense.

3.4 Numerical implementation

The numerical implementation of the Stokes BEM solver described in the previous section is based on our Laplace BEM solver [11], [12]. The Stokes solver source code is freely available online. Scan the adjacent QR code to access the repository. In the following we describe the main features of the developed algorithm. The boundary element method requires discretization of only the boundary surfaces in a three-dimensional domain. There are several methods and algorithms to create such surface discretisations and output the computational mesh in a readable format. An open source solution called *gmsh* [13] was chosen as the primary mesher for our method. It produces high quality triangular or quadratic meshes that are perfect for use with the boundary element method.

The integrals in eqn (14) depend solely on the mesh geometry and can be calculated for each computational mesh and stored. As we performed more than 1500 simulations using the same geometry of the particle, storing of integrals in binary form on a hard drive are reusing them for simulations with different boundary conditions saves a lot of compute time.

We used meshes with triangular elements featuring linear interpolation of functions across the surface and constant interpolation of boundary traction. Integration over triangles in 3D space was performed numerically. We used the barycentric coordinate system. The weights and positions of the numerical quadrature were chosen according to Wandzurat and Xiao [14]. For the evaluation of regular integrals a machine exact quadrature for polynomials of degree 25 was chosen. To increase the integration accuracy of singular integrals, we used the element decomposition technique. Each triangular element is decomposed into four triangles so that each triangle contains a possible singularity point (the three corners for linear interpolation or the barometric centre for constant interpolation). This decomposition is recursively applied to the singular point. Ten recursive steps were used for the simulations in this paper. They were chosen so that the accuracy of the singular integrals is of the same order of magnitude as the accuracy of the regular integrals.

Once the system of linear equations is established, we solve it using the iterative least squares method (Paige and Saunders [15]). The solution of the linear system of equations provides the boundary tractions on the particle surface. On this basis, the resulting force and torque (eqn (1)) are estimated by numerical quadrature as described above.

4 RESULTS

We set up the computational domain and boundary conditions as shown in Fig. 2. The particle is located in the centre of the domain and is surrounded by a spherical outer surface whose diameter is much larger than the size of the particle. Velocity boundary conditions are applied to the outer sphere according to the known flow field and the position of the particle in the flow field. No slip velocity boundary condition is used at the particle surface. The boundary

tractions at the particle surface and at the outer sphere are unknown and are obtained when the system of linear equations is solved.

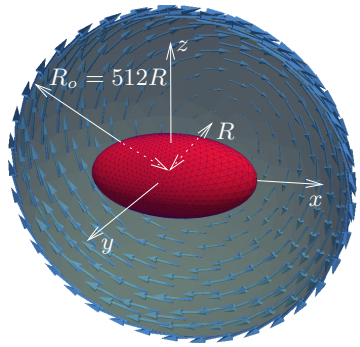

Figure 2: A particle and the flow field boundary condition on the on the outer surface of the domain. Volume equivalent radius of the particle is denoted by R. No slip boundary condition is applied at the particle surface. The arrows at the outer surface denote an example of a prescribed velocity field (vortex around the y axis). The radius of the outer sphere is R_o.

4.1 Validation with ellipsoidal particle

To validate our approach we first consider three standard flows: the plug flow along the three axes of the particle FoR, pure vortices around the three axes of the particle FoR, and three pure strains around the three axes of the particle FoR. Plug flow can be expressed as $\vec{w} = v_0(1, 0, 0)$, $\vec{w} = v_0(0, 1, 0)$, and $\vec{w} = v_0(0, 0, 1)$ for the three axes respectively. Vortical flows are $\vec{w} = v_0/L(0, -z, y)$, $\vec{w} = v_0/L(z, 0, -x)$, $\vec{w} = v_0/L(-y, x, 0)$ for a vortex around the x, y and z axis. Finally, pure strain can be applied on the particles by putting them into the following flow field $\vec{w} = v_0/L(0, z, y)$, $\vec{w} = v_0/L(z, 0, x)$, $\vec{w} = v_0/L(-y, x, 0)$ for x, y and z axis, respectively. In all these cases we consider the particle to be located at the origin.

We consider a particle in the form of a $2 : 1 : 1$ ellipsoid whose long axis is twice as long as the short axis. For such prolate ellipsoid, the expressions for force and torque in the Stokes flow are available in closed form from Jeffery [16] and Ravnik et al. [17]. We measure the relative error of drag force and torque as $abs(|\vec{F_n}| - |\vec{F_a}|)/|\vec{F_a}|$, and $abs(|\vec{T_n}| - |\vec{T_a}|)/|\vec{T_a}|$, where subscripts n and a stand for numerical and analytical solution, respectively.

In Fig. 3 we show the relative errors. Considering the drag force error in plug flow, we find that it depends strongly on the domain size. Only at $R_o/R = 2000$ the error converges to 10^{-3}, which we consider acceptable. A large domain size is easily achieved by BEM, while domain based methods struggle with it [18]. We also note that the torque error in vortex and strain flows does not depend on the domain size. But it does depend on the discretization of the particle. For all torques, the error is smaller than 10^{-3} when at least 3000 nodes are used in the discretisation of the particle.

4.2 Muscovite mineral particle in pipe, Poiseuille and Arnold–Beltrami–Childress flows

Strohmeier et al. [1] studied an air sample from Libby, a town in northwestern Montana, United States, where nearby vermiculite mines contaminated the air with asbestos and asbestos-like fibres. They discovered and analysed an irregular muscovite mineral particle

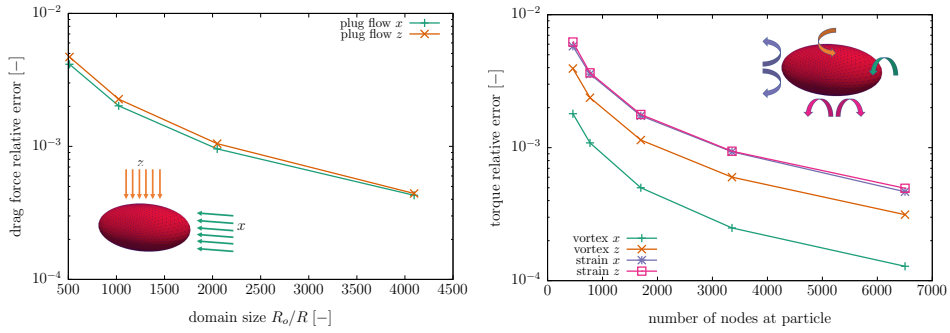

Figure 3: Left: relative error of the drag force estimate under plug flows from two directions versus the size of the domain. Right: relative error of the torque estimate for two vortex flows and two strain flows.

(hydrated aluminium potassium silicate $KAl_2(AlSi_3O_{10})(F,OH)_2$), which counts as an asbestos fibre. Based on their TEM images, we created a 3D model. At first glance, an elongated ellipsoid with an aspect ratio of 6.5 seems to correspond well to the particle. However, a closer look reveals that the real muscovite particle is irregular and asymmetrical. In Fig. 4 we present a 3D view of the two shapes. The volume of both particles is the same.

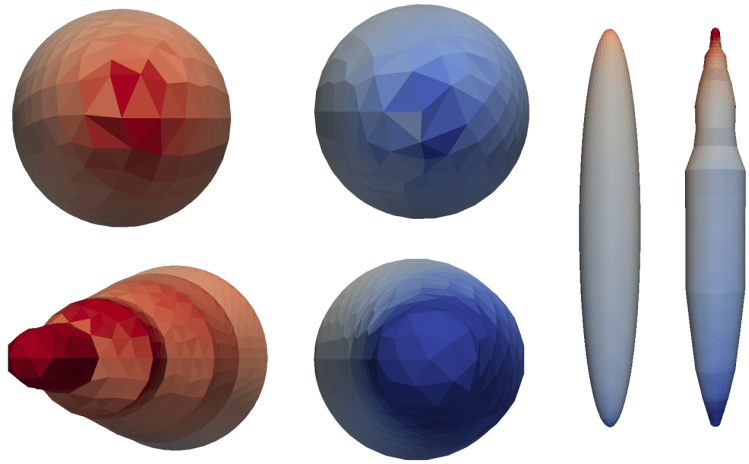

Figure 4: The x component of boundary traction shown at the surface of muscovite and ellipsoid particles. Top view is shown on the left, bottom view in the centre and side view on the right.

To quantify the difference in evaluated force and torque between a model of a muscovite particle and its simplifying ellipsoidal approximation, we place the particle in a flow in a pipe, a Poiseuille flow and an Arnold–Beltrami–Childress flow. Table 1 shows the details of the velocity fields and the proposed particle positions. For a given particle orientation, we then simulate the flow field and calculate the force and torque exerted by the fluid on

the particle. An example of such results can be found in Fig. 4, where a component of the boundary traction on the surface of the muscovite and ellipsoidal particles is shown for a single orientation of a particle in pipe flow.

Table 1: Linearization of the velocity field for flow in a pipe, Poiseuille flow and Arnold–Beltrami–Childress flow. Fluid viscosity is μ, pipe diameter D, distance between plates H, size of ABC cell L, k is the pressure drop, v_0 is the characteristic (average) flow velocity and ν the ABS flow frequency. $\vec{r}$ denotes the position of the particle in the flow field.

$\vec{v}$	$\vec{\nabla}\vec{v}$	$\vec{w}$
Steady laminar flow in a pipe, $\vec{r}_p = (0, D/4, D/4)$, $v_0 = \frac{kD^2}{32\mu}$		
$\begin{pmatrix} 2v_0\left(1 - 4\frac{y^2+z^2}{D^2}\right) \\ 0 \\ 0 \end{pmatrix}$	$16\frac{v_0}{D}\begin{pmatrix} 0 & -\frac{y}{D} & -\frac{z}{D} \\ 0 & 0 & 0 \\ 0 & 0 & 0 \end{pmatrix}$	$v_0\begin{pmatrix} 1 - 4\frac{y+z}{D} \\ 0 \\ 0 \end{pmatrix}$
Poiseuille flow in 2D, $\vec{r}_p = (0, 0, H/4)$, $v_0 = \frac{H^2 k}{12\mu}$		
$\begin{pmatrix} 6v_0\frac{z}{H}\left(1 - \frac{z}{H}\right) \\ 0 \\ 0 \end{pmatrix}$	$\begin{pmatrix} 0 & 0 & 6\frac{v_0}{H}\left(1 - 2\frac{z}{H}\right) \\ 0 & 0 & 0 \\ 0 & 0 & 0 \end{pmatrix}$	$v_0\begin{pmatrix} \frac{9}{8} + 3\frac{z}{H} \\ 0 \\ 0 \end{pmatrix}$
Arnold–Beltrami–Childress flow, $\vec{r}_p = (1/4, 1/4, 1/4)$, $A \to 1, B \to 2, C \to 3, \nu \to 2\pi$		
$v_0\begin{pmatrix} A\sin(\nu z/L) + C\cos(\nu y/L) \\ B\sin(\nu x/L) + A\cos(\nu z/L) \\ C\sin(\nu y/L) + B\cos(\nu x/L) \end{pmatrix}$	$-\frac{v_0}{L}\begin{pmatrix} 0 & 6\pi & 0 \\ 0 & 0 & 2\pi \\ 4\pi & 0 & 0 \end{pmatrix}$	$v_0\begin{pmatrix} 1 - 6\pi y/L \\ 2 - 2\pi z/L \\ 3 - 4\pi x/L \end{pmatrix}$

We performed 515 simulations for each flow type. Defining the flow as described in Table 1 we rotated the particle by setting the Euler parameters using the following algorithm:

for e_0 in range -1 to $+1$ with step 0.2
  for e_1 in range -1 to $+1$ with step 0.2
    for e_2 in range -1 to $+1$ with step 0.2
      $e_3 = \sqrt{1 - e_0^2 - e_1^2 - e_2^2}$
      if $e_3 \leq 1$ then perform simulation and estimate force and torque

The relative error between the force and torque obtained from the ellipsoidal approximation of the muscovite particle and the numerical simulation of the actual particle was estimated for all orientations j by:

$$E_{Fi}^{(j)} = \left| \frac{F_{i,num}^{(j)} - F_{i,ell}^{(j)}}{F_{i,num}^{(j)}} \right|, \qquad E_{Ti}^{(j)} = \left| \frac{T_{i,num}^{(j)} - T_{i,ell}^{(j)}}{T_{i,num}^{(j)}} \right|. \tag{21}$$

A probability density function (PDF) for the relative error was created. In Fig. 5 we show the integrals of the PDFs over the relative error. From this plot, we can see that the probability of estimating the force on a muscovite particle in a pipe flow with a relative error of less than

10% is between 10%–30% for the three force components. At the same time, we see that in about 20% of the orientations, the force is estimated with relative error greater than 100%. The results are more promising in the case of torque, where, for example, the x component is estimated with less than 10% error in 80% of orientations. If we look at the plots for Poiseuille and ABC flow, we come to similar conclusions. In the ABC flow case, the force is estimated with less than 10% error in only 10% of the orientations, which is worse than in the Poiseuille case, where the same accuracy is obtained for 20%–40% percent orientations. The largest errors are observed when considering the torque about the long (x) axis. This is due to the fact that the muscovite particle is extremely asymmetric about the long axis and deviates greatly from the ellipsoidal shape.

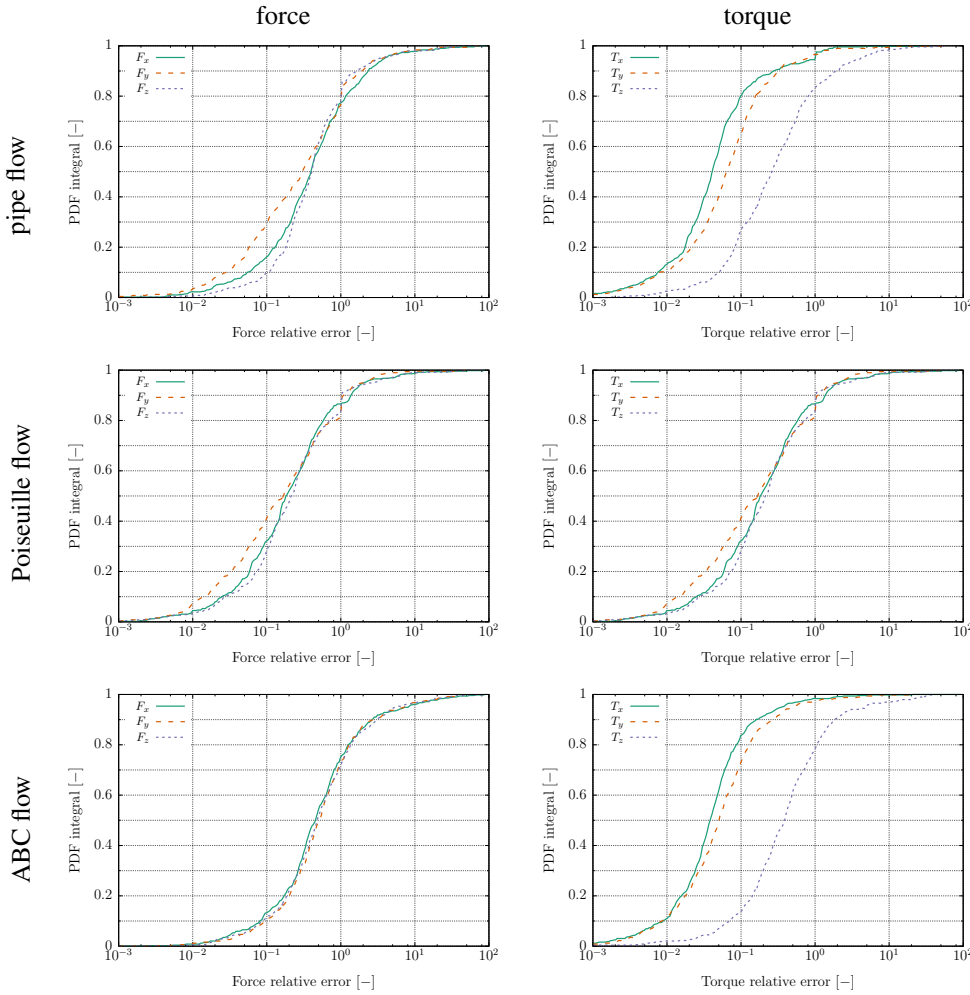

Figure 5: Integral of the PDF for the relative error in prediction of force and torque.

5 CONCLUSIONS

We have developed a boundary element method for solving force and torque exerted on arbitrarily shaped particles in Stokes flows. It is applicable to situations where the Reynolds number of the particles is small, so that creeping flow conditions exist around the particles. The developed method was used to compare the predicted force and torque values on a realistic 3D model of an asbestos particle and its simplifying ellipsoidal approximation. We found that the force and torque calculated for the real particle geometry differed greatly from the values obtained with the ellipsoidal approximation.

It seems that the use of analytical expressions available for ellipsoidal particles performs poorly in predicting the force and torque of a real particle. Analytical expressions are often used in Lagrangian particle tracking applications because the force and torque for many particles need to be evaluated in many time steps. In the future, we will use fast BEM approaches to reduce computational time so that the BEM solution of force and torque can be coupled with computational fluid dynamics solvers that perform particle tracking in flows.

REFERENCES

[1] Strohmeier, B.R., Huntington, J.C., Bunker, K.L., Sanchez, M.S., Allison, K. & Lee, R.J., What is asbestos and why is it important? Challenges of defining and characterizing asbestos. *International Geology Review*, **52**(7–8), pp. 801–872, 2010.

[2] Tavakol, M.M., Ghahramani, E., Abouali, O., Yaghoubi, M. & Ahmadi, G., Deposition fraction of ellipsoidal fibers in a model of human nasal cavity for laminar and turbulent flows. *Journal of Aerosol Science*, **113**(March), pp. 52–70, 2017.

[3] Shachar-Berman, L., Ostrovski, Y., De Rosis, A., Kassinos, S. & Sznitman, J., Transport of ellipsoid fibers in oscillatory shear flows: Implications for aerosol deposition in deep airways. *European Journal of Pharmaceutical Sciences*, **113**(September 2017), pp. 145–151, 2018.

[4] Kiasadegh, M., Emdad, H., Ahmadi, G. & Abouali, O., Transient numerical simulation of airflow and fibrous particles in a human upper airway model. *Journal of Aerosol Science*, **140**(May 2019), 105480, 2020.

[5] Cressey, B.A. & Whittaker, E.J.W., Five-fold symmetry in chrysotile asbestos revealed by transmission electron microscopy. *Mineralogical Magazine*, **57**(389), pp. 729–732, 1993.

[6] Bonifazi, G., Capobianco, G. & Serranti, S., Asbestos containing materials detection and classification by the use of hyperspectral imaging. *Journal of Hazardous Materials*, **344**, pp. 981–993, 2018.

[7] Pascolo, L. et al., Synchrotron soft X-ray imaging and fluorescence microscopy reveal novel features of asbestos body morphology and composition in human lung tissues. *Particle and Fibre Toxicology*, **8**, pp. 1–11, 2011.

[8] Wille, G., Lahondere, D., Schmidt, U., Duron, J. & Bourrat, X., Coupling SEM-EDS and confocal Raman-in-SEM imaging: A new method for identification and 3D morphology of asbestos-like fibers in a mineral matrix. *Journal of Hazardous Materials*, **374**(March), pp. 447–458, 2019.

[9] Pozrikidis, C., *Introduction to Theoretical and Computational Fluid Dynamics*, Oxford University Press: USA.

[10] Ingber, M.S. & Li, J., Surface pressure solution for boundary-element analysis of Stokes flow. *Communications in Applied Numerical Methods*, **7**(August 1990), pp. 367–376, 1991.

[11] Šušnjara, A., Verhnjak, O., Poljak, D., Cvetković, M. & Ravnik, J., Stochastic-deterministic boundary element modelling of transcranial electric stimulation using a three layer head model. *Engineering Analysis with Boundary Elements*, **123**, pp. 70–83, 2021.
[12] Šušnjara, A., Verhnjak, O., Poljak, D., Cvetković, M. & Ravnik, J., Uncertainty quantification and sensitivity analysis of transcranial electric stimulation for 9-subdomain human head model. *Engineering Analysis with Boundary Elements*, **135**, pp. 1–11, 2022.
[13] Geuzaine, C. & Remacle, J.F., Gmsh: A 3-D finite element mesh generator with built-in pre- and post-processing facilities. *International Journal for Numerical Methods in Engineering*, **79**(11), pp. 1309–1331, 2009.
[14] Wandzurat, S. & Xiao, H., Symmetric quadrature rules on a triangle. *Computers and Mathematics with Applications*, **45**(12), pp. 1829–1840, 2003.
[15] Paige, C.C. & Saunders, M.A., LSQR: An algorithm for sparse linear equations and sparse least squares. *ACM Transactions on Mathematical Software*, **8**, pp. 43–71, 1982.
[16] Jeffery, G., The motion of ellipsoidal particles immersed in a viscous flow. *Proceedings of the Royal Society A*, **102**, pp. 161–179, 1922.
[17] Ravnik, J., Marchioli, C. & Soldati, A., Application limits of Jeffery's theory for elongated particle torques in turbulence: A DNS assessment. *Acta Mechanica*, 2017.
[18] Štrakl, M., Wedel, J., Steinmann, P., Hriberšek, M. & Ravnik, J., Numerical drag and lift prediction framework for superellipsoidal particles in multiphase flows. *International Journal of Computational Methods and Experimental Measurements*, **10**(1), pp. 38–49, 2022.